ACCSCIENCE PUBLISHING

Materials Science in Additive Manufacturing

ORIGINAL RESEARCH ARTICLE

Enhanced strength of A131 steel via heterostructures induced by laser-directed energy deposition

Yuchao Bai[1,2,3], Silu Zhang[1,2,3], Qi Yan[1,2,3]*, Cuiling Zhao[1,2,3]*, and Jiaming Zhan[4]

[1]Guangdong Provincial Key Laboratory of Intelligent Morphing Mechanisms and Adaptive Robots, Harbin Institute of Technology, Shenzhen, Guangdong, China

[2]Key University Laboratory of Mechanism and Machine Theory and Intelligent Unmanned Systems of Guangdong, Harbin Institute of Technology, Shenzhen, Guangdong, China

[3]School of Robotics and Advanced Manufacture, Harbin Institute of Technology, Shenzhen, Guangdong, China

[4]School of Advanced Manufacturing, Sun Yat-sen University, Shenzhen, Guangdong, China

(This article belongs to the *Special Issue: Metallic Additive Manufacturing*)

Abstract

The trade-off between strength and plasticity has posed a challenge to the broader application of conventional metallic structural materials in high-speed, heavy-load, and extreme service environments. Heterogeneous structure designs could potentially overcome these limitations with their inherent superior combination of strength and plasticity. To harness this potential, this study employed a directed energy deposition additive manufacturing (AM) technology to fabricate a novel heterostructure in as-built (AB) A131 steel, consisting of alternating coarse and fine-grain layers along the building direction. In addition, a heat treatment process was applied to fabricate a near-homogeneous microstructure, allowing for the investigation of the role of crystal misorientation in tensile anisotropy. Compared to the performance of commercial hot-rolled ASTM A131 steel (yield strength [σ_{YS}]: 346.5 MPa; ultimate tensile strength [σ_{UTS}]: 545.0 MPa), the AB A131 steel achieved significant enhancements of 168.3% and 78.0% in σ_{YS} and σ_{UTS}, respectively, when maintaining a comparable elongation of 24.6% along the deposition direction similar to the ASTM A131 standard. Comprehensive experimental characterizations, combined with molecular dynamics simulations, were conducted to investigate the underlying formation mechanism of the heterostructure and the origins of mechanical anisotropy. It was found that single-pass deposition produced three distinct microstructure regions with different grain sizes owing to dendrite growth. With repeated thermal cycles, these evolved into a layered heterostructure consisting of alternating fine crystals and coarse-columnar grains. This heterostructure remarkably contributed to an exceptional improvement in strength, accompanied by only a minor reduction in plasticity. These findings present an efficacious avenue for substantially augmenting the mechanical properties of conventional iron-based alloys, offering useful references for overcoming the strength-plasticity trade-off in other alloys fabricated by AM.

Keywords: Additive manufacturing; A131 steel; Heterostructure; Mechanical performance; Molecular dynamics

***Corresponding authors:**
Qi Yan
(galaxy.yanqi@gmail.com)
Cuiling Zhao
(zhaocuiling@hit.edu.cn)

Citation: Bai Y, Zhang S, Yan Q, Zhao C, Zhan J. Enhanced strength of A131 steel via heterostructures induced by laser-directed energy deposition. *Mater Sci Add Manuf*. 2025;4(3):025220038. doi: 10.36922/MSAM025220038

Received: May 27, 2025

Revised: June 14, 2025

Accepted: June 16, 2025

Published online: July 21, 2025

Copyright: © 2025 Author(s). This is an Open-Access article distributed under the terms of the Creative Commons Attribution License, permitting distribution, and reproduction in any medium, provided the original work is properly cited.

Publisher's Note: AccScience Publishing remains neutral with regard to jurisdictional claims in published maps and institutional affiliations.

1. Introduction

Additive manufacturing (AM) has demonstrated ultra-high efficiency in producing heavy-load, complex-geometry, and large-volume equipment, exemplified by the successful launch of Terran 1, a launch vehicle entirely manufactured by 3D printing, primarily using directed energy deposition (DED) technology.[1] The 2-month production cycle of the 3D-printed rocket set a new record for the fastest rocket fabrication in history. Large-format metallic structural components developed using the DED method have been widely employed in alloys, such as titanium,[2] aluminum,[3] copper,[4] iron,[5] and their matrix composites.[6] Since the rapid commercialization and development of the aviation industry, difficult-to-machine alloys (*e.g.*, titanium alloys) have struggled to meet the demands of resource-efficient manufacturing. The outstanding performance of the Falcon[7] heavy-launch vehicle outlined that conventional high-strength steel could also be used in space equipment with remarkable economic effects. As a result, conventional iron materials are gaining increasing attention for future applications in the commercial aerospace industry.

A131 steel, a distinctive low-carbon structural steel developed over the past century, typically exhibits a standard yield strength of 235~390 MPa and an elongation of 19~23%, occupying a significant share in the steel market due to its comprehensive applications in both civilian and defensive industries, especially in marine vessels.[5,8,9] However, the structural strength of conventional A131 steel lacks the strength of conventional aerospace titanium alloy (*e.g.*, 800~1200 MPa for Ti-6Al-4V [Ti64]).[10,11] Leveraging the rapid cooling rates associated with laser melting to introduce the formation of martensite phases offers a promising route to enhancing the strength of the A131 steel.[5,12,13] Wu *et al.*[14,15] employed a selective laser melting method, combined with post-treatment, to fabricate A131 steel. Their results demonstrated a significant enhancement in strength, with the as-built (AB) A131 steel achieving a tensile strength of 1030 MPa, comparable to that of Ti64 alloy. However, this enhancement was accompanied by a reduction in plasticity, as the elongation of the A131 steel dropped sharply to just 3%. Post-process heat treatment led to a partial recovery of elongation, albeit with a notable decrement in strength. Similarly, Wang *et al.*[16-18] also manufactured A131 steels using a selective laser melting method with various scanning strategies. The results revealed the formation of substantial martensite microstructures, with an improved tensile strength of 937 MPa and a notable reduction in elongation (*i.e.*, <6%). Although steel strength can be significantly improved through selective laser melting methods, it is often accompanied by a considerable loss in elongation, rendering the mechanical performance insufficient to match that of commercial aerospace alloys.

Constructing a heterogeneous microstructure with a dual-phase or dual-grain-size structure offers a promising strategy for enhancing the strength of A131 steel without reducing plasticity.[19,20] Due to the high freedom and the ability to deposit multimaterial parts with different powders,[21-23] the DED technique enables the development of special heterostructures to improve the performance of the materials.[24-26] For example, Dan *et al.*[27] developed heterogeneous TiAl alloys by alternately depositing Ti and TiAl layers using DED methods, achieving a significant improvement in plasticity compared to that of the heterogeneous TiAl alloy in a submicron scale. However, the heterogeneous structure still exhibited the inherent trade-off between strength and plasticity. Wu *et al.*[28] successfully fabricated a heterogeneous structure in lamella-structured titanium alloys, consisting of alternating coarse and fine-grain regions, through post-treatment processes. This design led to a remarkable improvement in tensile strength with a limited reduction in elongation. Similarly, Li *et al.*[29] reported the fabrication of heterostructures in titanium alloys composed of alternating coarse and fine grains via a heat-treatment (HT) process. The results demonstrated a noticeable improvement in strength when maintaining elongation comparable to that of the control group. Gao *et al.*[20,30] fabricated heterostructures in SS316L steel via selective laser melting using an alternating remelting method. Their resulting heterostructure comprised nanoscale alternating layers of recrystallized and non-recrystallized regions, achieving a notable improvement in ultimate tensile strength with a limited decrement in elongation. Su *et al.*[26] designed DED processes incorporating interlayer pauses to fabricate maraging steels with heterogeneous layers composed of multiple phases in alternating layers, achieving a super-high strength of 1.5 GPa in maraging steel. These findings suggest that if a heterogeneous structure consisting of alternating coarse and fine-grain layers could be controlled by an AM method, the A131 steel could also potentially overcome the trade-off effects of strength and plasticity in a cost-effective manner. Although selective laser melting has demonstrated the feasibility of constructing nanoscale heterogeneous structures to overcome the trade-off effects, it has limited capabilities in fabricating complex geometries on a large scale. Therefore, developing DED methods to construct a submicron heterostructure with varied grain sizes is a promising strategy for achieving simultaneous improvements in both strength and plasticity, particularly for future applications in large-scale engineering equipment.

In this study, A131 steel with heterostructures, comprising alternating layers of coarse and fine grains, was successfully developed using a DED method that utilizes the dendritic growth features of melt pools and thermal cycle behavior. An HT and commercial hot-rolled (HR) A131 steel was also employed in this study as the control group. The tensile strength of the AB A131 steel exhibited an exceptional combination of strength, approaching that of Ti64 alloy, and plasticity within the range specified by the ductile ASTM A131 standard. To understand the formation mechanism of the heterostructure, multitype microstructure characterization and single-pass deposition experiments were employed to elucidate the model of the alternating layer of fine and coarse grains with crystal misorientation. In addition, molecular dynamics (MD) was employed to reconstruct the model of the heterogeneous microstructure according to the observed microstructure. The model was stretched in the same direction as the experimental process to reveal the anisotropy of the tensile behavior of the AB A131 steel. This innovative structural design strategy presents a promising insight into crafting traditional iron with a remarkable strength-plasticity combination free from trade-off effects, with broader implications for other conventional alloys in the industries.

2. Materials and methods

2.1. Materials

In this study, commercial gas-atomized mild steel powders (A131 EH36; particle size: 45 – 90 μm; Zhongyuan Advanced Materials Technology Co., Ltd, China) were utilized (Figure 1A). The powder was approximately spherical, with a low-carbon equivalent value (0.3%) (Figure 1B; Table S1). For comparison, commercial HR A131 steel bulk (ThyssenKrupp Material Services GmbH Co., Ltd., Germany) was used as the control group. All materials were used in the as-received state.

2.2. Fabrication process

The AB A131 EH36 steel used in this study was fabricated using a DED AM machine (Figure 2A) equipped with a fiber laser (wavelength: 1070 nm; laser beam spot diameter: 2.5 mm) under an argon atmosphere (1 bar pressure). The DED settings were: 1.23 kW laser power, 0.5 mm layer thickness, 1200 mm/min moving speed, 1.25 mm track space, and 722.2 mm/min powder feeding speed with Gaussian distribution. The orthogonal strategy was used, where the moving direction rotated by 90° for each alternating layer alongside the building direction (Figure 2B). To distinguish the building direction, a 3D axis was constructed with normal direction (ND; parallel to the laser deposition), transverse direction (TD), and rolling direction (RD).

In the HT process, the AB A131 EH36 steel was quenched and subsequently tempered using a box-type furnace (MXQ1600-40, MICRO-X Ltd Co., China) (Figure 2C). The cleaned AB A131 EH36 bulk was heated (10 K/min) at 910°C for 0.5 h, followed by water quenching, subsequent tempering at 500°C for 2 h (Figure 2D), and air-cooling. To investigate the formation mechanism of the microstructure, single-pass deposition of A131 steel was carried out using the DED method with the same parameters.

2.3. Material characterization

The starting raw materials and bulks were characterized using a scanning electron microscope (SEM) (JEOL JSM-5500LV; JEOL Ltd., Japan) equipped with an energy-dispersive X-ray spectrometer (EDS). The microstructure of the bulks was also examined using an SEM system (Apreo 2 SEM; Thermo Fisher Scientific, United States of America [USA]) equipped with EDS and an electron backscatter diffraction (EBSD) detector. The microstructure was also observed using a laser confocal

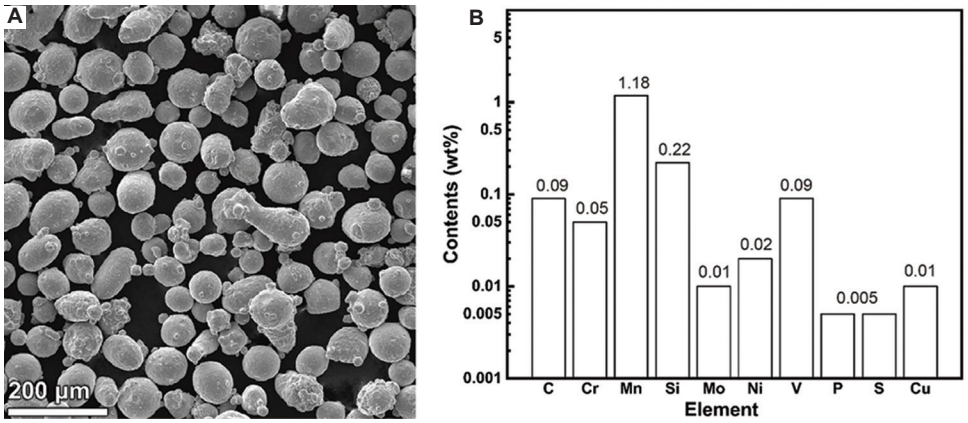

Figure 1. Steel powder morphology (A) and elemental composition (B)

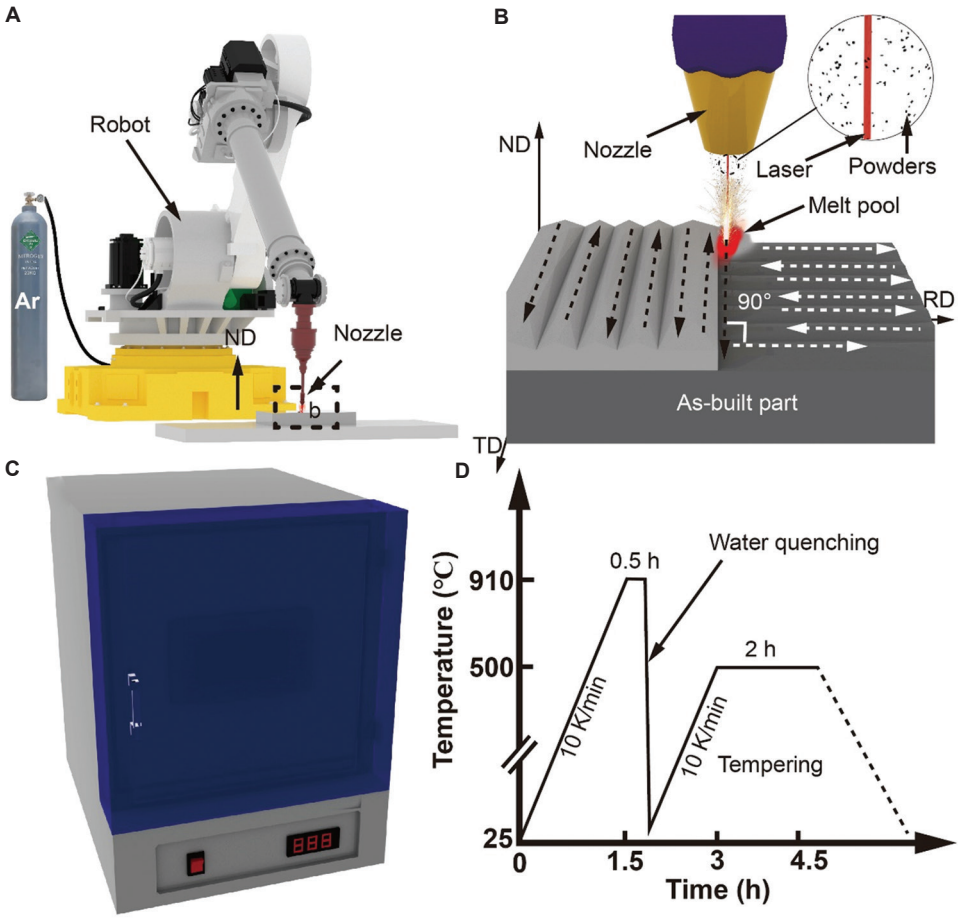

Figure 2. Diagrams of material fabrication and post-treatment process: (A) Schematics of the L-DED process; (B) manufacturing strategy; (C) oven used for heat treatment; and (D) heat treatment parameters
Abbreviations: L-DED: Laser-directed energy deposition; ND: Nominal direction; TD: Transverse direction; RD: Rolling direction

microscope (Olympus LEXT OLS5000; Alpha Co., USA). For SEM observation, the surface of the bulk was ground and polished in accordance with ASTM E3-2011 standards, followed by etching with an ethylene nitrate mixture (4 mL HNO_3 and 100 mL C_2H_5OH). For EBSD examination, the surface of the bulk was electrolytically polished in accordance with ASTM E1558 standards using a 1 μm step referring to GB/T 36165-2018.[31]

Phase analysis was performed using X-ray diffraction (XRD) (SmartLab SE; Rigaku Co., Ltd., Japan) with the CoKa wavelength (λ_{Co} Ka) of 1.79 Å, over a rotation-diffraction angle of 30° – 120° and a scanning speed of 5°/min. The density of all AB bulks was measured using the Archimedes method (ISO 1183-2017) in an analytical reagent grade alcohol solution.

2.4. Material property testing

The uniaxial tensile (ISO 6892-1: 2009) and Vicker hardness test (ISO 6507-1-2018) were carried out at room temperature to evaluate the material mechanical properties. The uniaxial tensile performance was examined using a microcomputer-controlled electronic universal testing machine (Instron 8501; INSTRON Co., USA) at a strain rate of 0.5 mm/min. The AB bulks were machined into a dog bone-shaped specimen, with a total length of 40 mm, thickness of 3 mm, gauge width of 4 mm, and gauge length of 12 mm. The hardness test was carried out using a Vickers hardness tester (HV-1000Z; HUAYIN Ltd., China) with a load of 200 gf and a dwell time of 15 s.

2.5. Models and computation

The model construction and analysis of deformation behavior during tensile loading were performed using MD simulations with the LAMMPS package.[32,33] This method has been successfully applied in assessing the mechanical performance of metals with body-centered cubic (BCC) crystal structures,[34,35] especially in iron-based materials.[36] The corresponding directions of the model along ND,

TD, and RD corresponded to the x-, y-, and z-axes, respectively. The entire configuration was box-shaped (43 × 11 × 43 nm), packed with two kinds of grains with the same lattice parameter of 2.86 Å. These two types of grains formed a sandwich structure: Fine equiaxed crystals with an average diameter of 2.86 nm at the edges, and coarse columnar grains in the center, measuring approximately 2.86 nm in diameter and 7 nm in length.

The entire system was first thermalized and equilibrated to zero pressure using the isothermal-isobaric ensemble (NPT) under 3D periodic boundary conditions. For the uniaxial tension simulation, all the samples were deformed either along the ND and TD axes at a constant strain rate of 1×10^9 s^{-1}. Periodic boundary conditions were applied along RD. For ND and TD, the tensile direction was set as "periodic," while the non-loading direction was assigned as "surface." In addition, zero normal stress was maintained along RD during deformation. Virial stresses in the tensile direction were calculated at each strain level. The engineering strain at each time step was calculated as:

$$\frac{l-l_0}{l} \quad \text{(I)}$$

where l and l_0 represent the length of the present and initial box along the tensile direction, respectively. The interaction between individual atoms in the Fe matrix was modeled using a many-body embedded-atom method based on the interatomic potential, which can be expressed as:

$$E_{tot} = \frac{1}{2}\sum_{ij} \mathrm{V}(r_{ij}) + \sum F(\bar{\rho}_i)$$
$$\bar{\rho}_i = \sum_{j \neq i} \rho(r_{ij}) \quad \text{(II)}$$

where $V(r_{ij})$ is the pair potential, r_{ij} is the atomic separation between j and i, F is the embedded energy as a function of $\bar{\rho}_i$, and $\rho(r_{ij})$ is the atomic function.

3. Results

3.1. Phase configuration and microstructure

Figure 3A displays the measured density and the relative density for the AB samples and control group, with the corresponding data summarized in Table S2. The measured density of all the steel bulks exceeded 7.7 g/cm^3 with minor variation, and the values of the AB steels were slightly higher than those of the control group. Compared to the theoretical density of A131 steel (7.85 g/cm^3), all the relative densities were above 98%, illustrating that both AB and HT steels were well-consolidated with minimal defects.

Figure 3B displays the XRD patterns of the steels, with similar peak profiles across A131 steels subjected to different post-processing treatments. This suggests that the crystal structure for the primary phase remained largely unchanged, consisting mainly of the ferrite (α-Fe) and/or martensite (α′), both of which possessed a BCC crystal structure.[17] The α′-phase was preferentially formed in the AB A131 steel due to non-equilibrium consolidation and rapid cooling rates (10^4 – 10^6 K/s) in the melt pool.[30] Subsequent treatments (HT or HR) facilitated the transformation of the α′-phase into α-Fe.[5] In addition, the most prominent diffraction peak corresponded to the crystal plane in all bulks, indicating a preferred crystallographic orientation, which might contribute to anisotropic mechanical performance.

Figure 4 displays the 3D-reconstructed optical microscope (OM) image of the AB bulk microstructure in an orthographic view. Figure 4A features the microstructure of AB A131 steel, revealing minor visible defects, such as holes and unfused particles, further confirming that the AB A131 steel was well-consolidated with full density. The grain size and grain profile were significantly different along ND and TD, which is due to dendritic growth during the consolidation of the melt pool.[37,38] In addition, there was a significant sandwich structure for the grain size in the TD section, a novel heterogeneous structure was formed layer-by-layer, consisting of coarse columnar grains and fine crystals, alongside the laser deposition direction. The layer thickness of columnar grains was ~300 μm, and fine acicular martensite and equiaxed crystals were observed, likely resulting from the high cooling rate and thermal cycles[30] induced by alternating laser deposition layers. Therefore, the imbalanced consolidation provided insufficient kinetics for the phase transformation from γ-Fe to α-Fe and pearlite, when promoting the formation of fine martensite.[39] In addition, the thermal cycle offered necessary thermodynamic advantages for the grain growth of fine crystals alongside ND, where a sandwich-heterostructure was formed, consisting of columnar grains and fine crystals. This heterostructure contributed to the anisotropy in grain orientation, consistent with the XRD results, and eventually induced variations in mechanical performance.

Following tempering, Figure 4B displays the microstructure of HT A131 steel, with significant variations observed for grain sizes and crystal profiles. The sandwich heterostructure was visible but disappeared when the grain size increased. The microstructure of HT A131 steel consisted of equiaxed grains with a typical ferrite-pearlite structure, indicating negligible variation in grain profiles alongside ND and TD. This

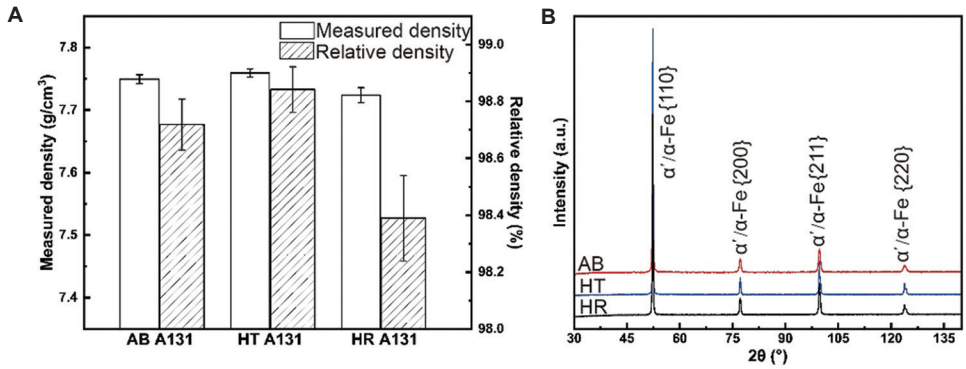

Figure 3. The density (n = 5) (A) and XRD patterns (B) of A131 samples subjected to different processes
Abbreviations: AB: As-built; HT: Heat treatment; HR: Hot rolling

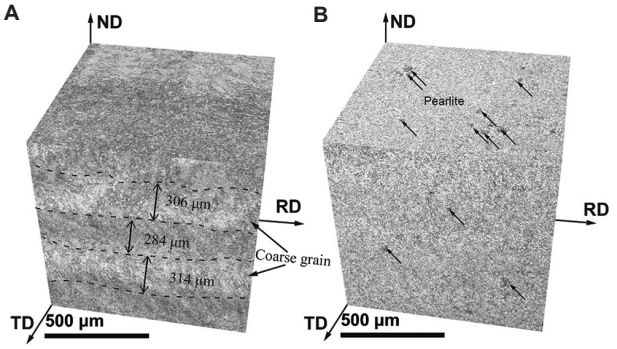

Figure 4. 3D-reconstructed microstructure of A131 steel: (A) AB; and (B) HT. Black arrows in (B) indicate pearlite
Abbreviations: AB: As-built; HT: Heat treatment; ND: Nominal direction; TD: Transverse direction; RD: Rolling direction

is most likely due to the HT process, which provided sufficient kinetic and thermodynamic conditions for both phase transformation and grain growth. In addition, the anisotropy of the microstructure was significantly reduced, which could be beneficial to the isotropic mechanical properties.

Figure 5A-C displays the magnified image of the AB A131 steel microstructure in the ND section. Figure 5A presents an OM image of the fine acicular martensite structure predominated with some coarse equiaxed grains (black arrows), and the acicular martensite possessed a submicron size without specific orientation (Figure 5A, inset). Figure 5B presents an SEM image of the acicular martensite-equiaxed grain structure with notable particle defects (white arrows). These particles (300~800 nm) were randomly distributed (Figure 5B, inset), most likely due to oxidation during the deposition process. As these particles were relatively small (<1 μm), their influence on density is negligible. The magnified SEM image (Figure 5C) highlights the submicron equiaxed grains (~2 μm) and acicular martensite blocks (~5 μm).

Figure 5D-F displays the AB A131 steel microstructure along the TD section at different magnifications. Figure 5D presents the transitional interface between the fine and coarse grains, where the boundary is not distinctive. The coarse-grain part mainly consisted of three types of grains: Coarse columnar grain, middle-size equiaxed crystal, and fine acicular martensite. The maximum length of the continued columnar reached 83.4 μm, surrounded by other small-sized grains. The dimension of equiaxed grains was measured as 16.5 μm, smaller than that of columnar grains (Figure 5D, inset). The size of the fine acicular martensite was the same as the grains in the fine grain region (Figure 5E). The boundary between the coarse- and fine-grain regions depended on the distribution of the columnar grains, and the fine grains primarily consisted of equiaxed grains and acicular martensite (Figure 5E, inset) in a submicron size. The magnified image (Figure 5F) reveals randomly distributed submicron defects and columnar grains as discontinuous lamellae along ND. This observation suggested that the heterogeneous structure was related to dendritic growth in the melt pools, resulting in partial grain coarsening.

To observe the AB A131 steel heterostructure, EBSD analysis was performed on the TD section. Figure 6A features an inverse pole figure (IPF) with grain orientations in different colors, revealing a non-uniform distribution and an optimal grain orientation consistent with the XRD results. According to grain size and grain profiles, the IPF image was divided into three parts (resembling a sandwich structure): Fine grain region (#1), coarse grain region (#2), and fine grain region (#3). The distribution of equivalent circle diameter for the relative regions is displayed in Figure 6B. The fine-grain region (#1) primarily consisted of acicular martensite and small equiaxed grains (average diameter: 6.91 μm), and the maximum diameter was <20 μm. Compared to region #1, grains in coarse grain

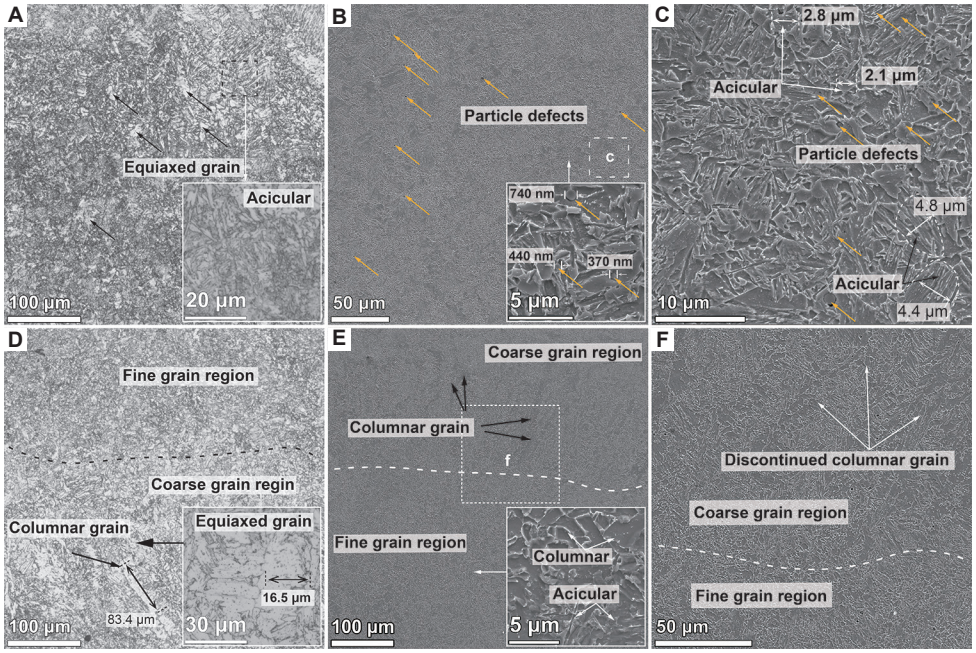

Figure 5. Microstructure of AB A131 along ND (A-C) and TD (D-F). Yellow arrow (B-C): Particle defects. Scale bars: 100 μm (A, D and E); 50 μm (B and F); 10 μm (C)
Abbreviations: AB: As-built; ND: Nominal direction; TD: Transverse direction

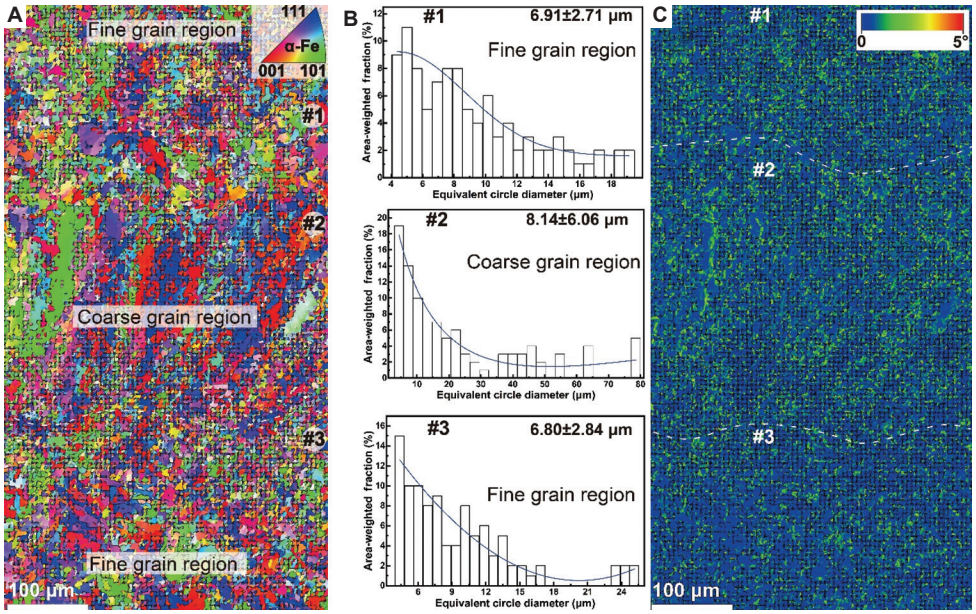

Figure 6. AB A131 steel heterostructure along TD: (A) IPF image; (B) grain size distribution, and (C) KAM mappings alongside the TD direction of AB A131 steel. Scale bars: 100 μm (A and C)
Abbreviations: AB: As-built; IPF: Inverse pole figures; TD: Transverse direction; KAM: Kernel average misorientation

region #2 have a larger average diameter of 8.14 μm and a maximum diameter of up to 80 μm, the increase in both parameters is likely due to the columnar grains. This further confirmed that the coarse-grain region primarily consisted of discontinued columnar grains formed by dendritic growth. In region #3, the average diameter of the grains was 6.8 μm (relatively similar to that of region #1), and the maximum diameter was <25 μm. This indicated that the fine-grain region mainly consisted of fine acicular martensite and small equiaxed grains.

Figure 6C displays the Kernel average misorientation (KAM) mappings, revealing the misorientation angle of the grains related to the lattice distortion. It can be observed that the misorientation was related to the grain size, with smaller grains exhibiting larger misorientation angles. A large misorientation angle corresponds to higher stress within the crystal, most likely due to the martensite phase and rapid cooling rates.

After tempering, the IPF mappings (Figure 7A) display equiaxed grains in HT A131 steel with uniformly distributed colors, suggesting reduced crystal misorientation compared to AB A131 steel. The corresponding pole figures (Figures S1 and S2) further confirmed that the HT process contributed to reducing the maximum orientation density of the grain (from 2.01° to 1.59°). In addition, the heterostructure disappeared, and both grain size and grain profiles became identical (average grain size: 7.93 μm), similar to that of the coarse grain region. This indicated that the HT process led to recrystallization, resulting in different orientations and the formation of equiaxed grains. Compared to AB A131 steel, the KAM mappings (Figure 7B) of HT A131 steel displayed smaller misorientation angles within the grains, likely due to reduced martensite content and grain growth, which helped reduce lattice distortion.

3.2. Mechanical properties

To further investigate the effects of A131 steel microstructure on mechanical performance, uniaxial tensile and hardness tests were performed along ND and TD, respectively. From the stress-strain curves (Figure 8A), AB A131 steel exhibited outstanding tensile strength compared to the other groups, while elongation significantly decreased compared to that of commercial steel along TD (HR-TD). In addition, AB A131 steel exhibited strong anisotropy in tensile strength, with both tensile strength and elongation of AB A131 steel along ND (AB-ND) surpassing those along TD (AB-TD). After the HT process, the performance of HT A131 steel tested along ND (HT-ND) also exceeded that along TD (HT-TD), suggesting that the HT process played a limited role in reducing anisotropy in mechanical performance. Moreover, an interesting Portevin-Le Chandelier (PLC) phenomenon[40,41] was observed in the curves of both AB-TD and HT-TD, leading to stress serrations in the curves. This observation is likely due to the negative strain rate sensitivity induced by dynamic strain aging effects,[42,43] where crystal misorientation of the grains led to increased dislocation interactions along TD under the given strain rate.

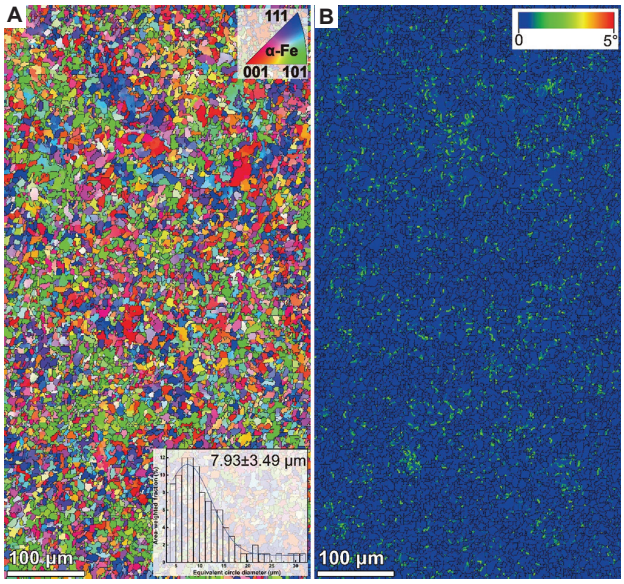

Figure 7. HT A131 steel heterostructure along TD: (A) IPF image; and (B) KAM mappings. (A, inset) a bar chart of the grainsize distribution. Scale bars: 100 μm

Abbreviations: HT: Heat treatment; IPF: Inverse pole figures; KAM: Kernel average misorientation; TD: Transverse direction

Figure 8B displays true stress-strain curves and corresponding work-hardening behavior based on Figure 8A, indicating that the work-hardening curve of HR-TD gradually decreases after the yield strength (σ_{YS}) point, with the rate of work-hardening declining gradually as elongation increases. The work-hardening rates of AB A131 steel decreased dramatically against the increasing rates of strains, especially for the AB-TD curve, likely due to limited elongation. Moreover, significant stress serrations were observed in the work-hardening curves along TD for both AB and HT A131 steel, attributed to the PLC effects, leading to notable stress fluctuations. This suggested that work hardening was limited in resisting deformation during the tensile test along TD at the given strain rate.

The corresponding σ_{YS}, ultimate tensile strength (σ_{UTS}), and elongation are displayed in Figure 8C, and the corresponding data are summarized in Table S3. Compared to the σ_{YS} (346.5 MPa) and σ_{UTS} (545.0 MPa) of HR-TD, the σ_{YS} and σ_{UTS} of AB-ND dramatically improved by 168.3% and 78.0%, respectively, with the strain of 24.6% meets the definition of the EH A131 standard (19~26% in strain). The performance of AB A131 steel decreased slightly in TD but reported enhanced σ_{YS} and σ_{UTS} of 132.2% and 46.6%, respectively, with a 65.5% reduction in elongation. This was attributed to the predominant acicular martensite and fine equiaxed grain (Figures 4-6), resulting in notable improvements in strength. After the HT process, HT A131 steel reported reduced strength, with enhancements of 70.0% and 24.1% in σ_{YS} and σ_{UTS}, respectively, for HT-ND, while HT-ND exhibited a 4.6% decrease in σ_{UTS}.

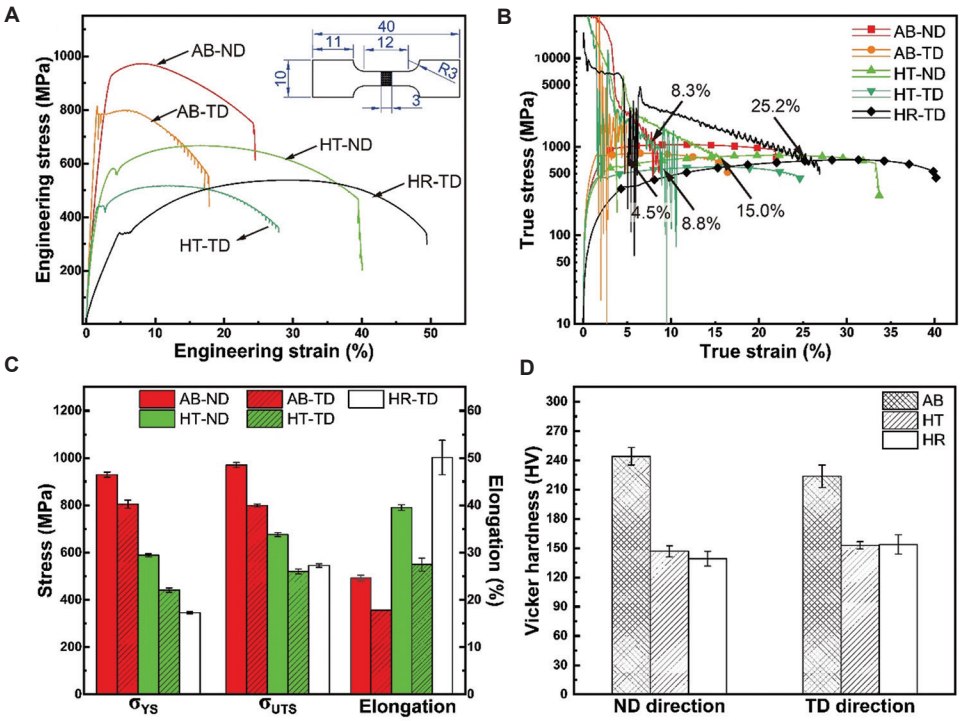

Figure 8. Room-temperature mechanism performances of A131 steel. (A) Room-temperature uniaxial strain-stress tensile curves. (B) True strain-stress tensile curves. (C) Tensile properties (n = 3). (D) Hardness (n = 10)
Abbreviations: AB: As-built; HR: Hot rolling; HT: Heat treatment; ND: Nominal direction; TD: Transverse direction

This observation was attributed to the elimination of fine martensite and the misorientation of the grains (Figure 7), leading to significant anisotropy in resistance deformation along the TD orientation.

Figure 8D displays the Vicker hardness of A131 steels along ND and TD, with corresponding values summarized in Table S4. All steels exhibited notable hardness anisotropy, with strength and elongation anisotropy ratios estimated in Table S5. In both AB and HT A131 steels, hardness was higher in ND compared to TD, whereas HR A131 steel displayed the opposite trend. Similar to the tensile results, AB A131 steel displayed the highest hardness, achieving a 75.5% increase over HR A131 steel in ND (139 HV). After HT, HT A131 steel exhibited a notable decrement in hardness in both directions, likely due to the formation of equiaxed grains with reduced misorientation. While HT A131 steel had a similar phase composition to HR A131, it offered only a marginal hardness advantage, though both retained higher anisotropy ratios than A131 steel fabricated using other DED methods[17] or wire-arc AM.[44]

Figure 9 presents the fracture morphologies of AB A131 steel along ND. Figure 9A displays the fracture surface at the edge close to the necking section, with numerous internal defects (white arrows). A magnified view (Figure 9B) reveals submicron holes (~20 μm) (Figure 9B, inset) surrounded by abundant dimples. These defects likely originated from small closed pores and inclusions inside the melt pools, which enlarged under tensile stress. Figure 9C highlights broken, spherical inclusions surrounded by dimples. EDS analysis (Figure 9C, inset) verified that these inclusions were rich in oxygen (> 50 at%), identifying them as oxide inclusions. Figure 9D features the middle of the fracture surface, also revealing visible holes (Figure 9E) and oxide inclusions (Figure 9F). These defects likely contributed to a significant decrease in elongation and a rapid decline in work-hardening rates. However, the prevalence of dimples indicates that plastic deformation remained predominant under tensile loading.

4. Discussion

In this experiment, AB A131 steel exhibited a unique heterogeneous structure composed of alternating coarse- and fine-grain regions, leading to significantly enhanced mechanical performance. To reveal the formation mechanism of the heterostructure, a single-pass deposition was carried out with the same DED parameters.

The overall cross-sectional microstructure is displayed in Figure S3, with high-magnification images presented in Figure 10. Figure 10A displays an OM image of the top region, revealing a notable orientation of the crystals

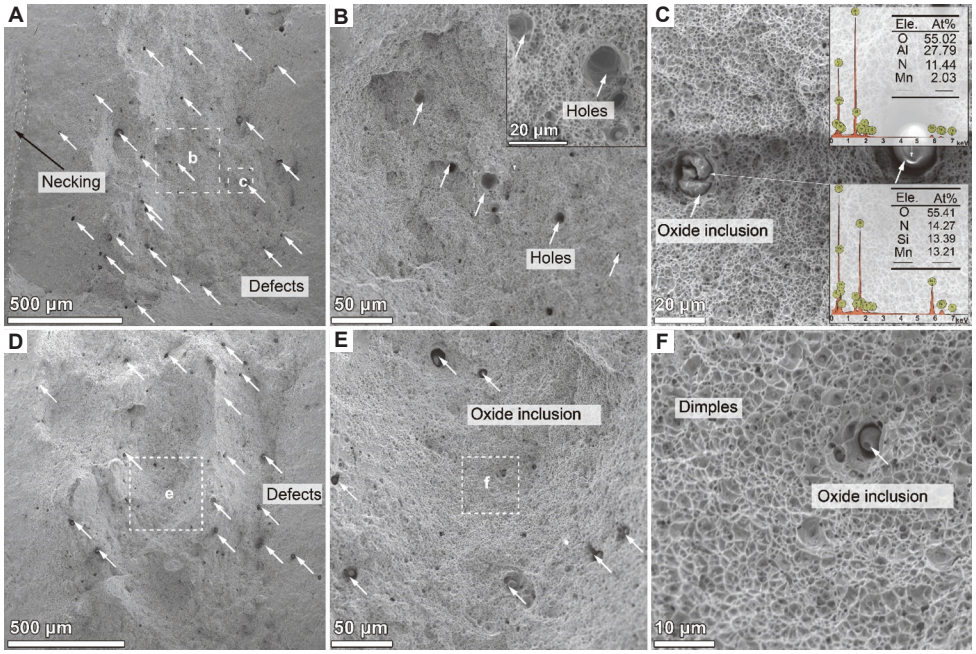

Figure 9. Broken surface of the tensile sample of AB A131 steel: (A-C) SEM images of defects at the edge; and (D-F) SEM images of defects in the middle. (C, inset) EDS spectrums of the particle defect. Scale bars: 500 μm (A and D); 50 μm (B and E); 20 μm (C); 10 μm (F)
Abbreviations: AB: As-built; SEM: Scanning electron microstructure; EDS: Energy dispersive spectrometer; O: Oxygen; Al: Aluminum; N: Nitrogen; Mn: Manganese

along ND. The grains were relatively small and comprised columnar grains, fine acicular martensite, and some equiaxed grains, attributed to dendritic growth during the consolidation of the melt pool under rapid cooling rates.[45] Discontinuous columnar crystals were formed along ND and surrounded by fine martensite. The IPF mappings (Figure 10B) further confirmed dendritic crystal formation along the build direction, consisting of columnar and fine-equiaxed grains with a weak (101) crystal orientation and a huge misorientation angle of 5.24° (Figure S4). The average equivalent grain size was 6.33 μm, with a maximum of 83.6 μm due to dendritic growth of the columnar grains.

Figure 10D displays the microstructure of the single-pass track in the middle region, featuring coarse columnar grains and acicular martensite. Compared to the top region (Figure 10A-C), the columnar grains are more evident (Figure 10E), indicating significant coarsening due to limited thermal conduction and a lower temperature gradient at the center of the melt pool.[46] This results in a discrepancy in grain size from the center to the edge, accompanied by increased crystal misorientation of 6.03° (Figure S5). The average grain size slightly decreased to 5.93 μm, but the maximum grain size significantly increased to 146.8 μm with a high area ratio (Figure 10F), substantially greater than in AB A131 steel (Figure 6). This suggests that alternating remelting and cyclic thermal effects helped refine the coarse columnar grains.

Figure 10G displays the microstructure at the interface between the single-pass track and the 304L steel substrate, consisting of equiaxed grains and acicular martensite. A distinctive interface could be observed, where fine A131 steel grains are deposited on the top of coarse 304L substrate grains. Compared to the microstructure of the single-pass track at the top (Figure 10A-C) and middle (Figure 10D-F) regions, the grains near the substrate (Figure 10H) resemble the fine-grained regions (Figures 4A; 5D and E; and 6), and the misorientation significantly decreased (Figure S6). The average grain size is approximately 5.45 μm (Figure 10I), slightly smaller than that of AB A131 steel (6.8 μm), with a maximum diameter of 31.6 μm. This suggests that laser thermal cycling promotes submicron-scale grain growth, leading to a slight increase in the average size. Such effects facilitate the formation of alternating fine- and coarse-grain regions during one-pass deposition. Subsequent passes remelt the surface with similar thermal gradients to those near the 304L substrate, promoting the formation of fined equiaxed crystals. These repeated thermal cycles contributed to the uniform distribution of heterogeneous structures at alternating layers.

To further investigate the heterostructure on anisotropic mechanical performance, an MD model of the sandwich structure was built, consisting of the fine- and columnar-grain regions with a similar volume ratio

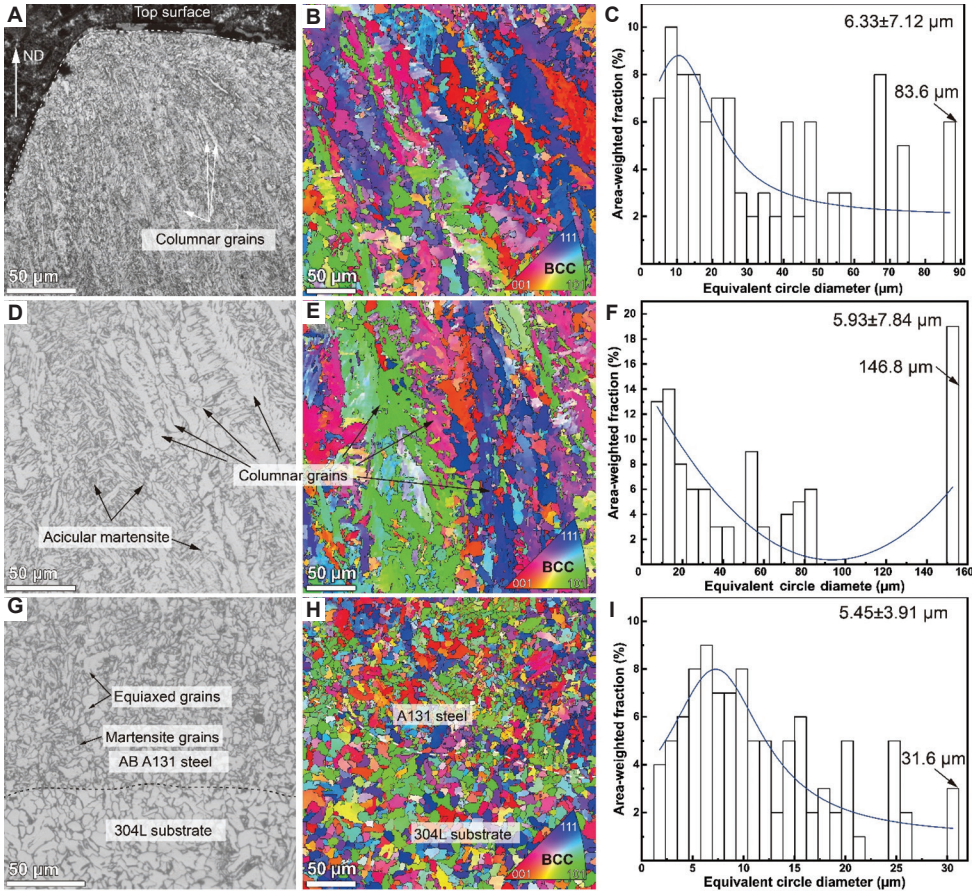

Figure 10. A131 steel microstructure from single-pass deposition: (A-C) top section; (D-E) middle region; and (G-I) bottom section. (A, D, G) OM image; (B, E, H) IPF image with corresponding grainsize distribution (C, F, I). Scale bars: 50 μm
Abbreviations: AB: As-built; BCC: Body centered cubic; IPF: Inverse pole figure; ND: Nominal direction; OM: Optical microscope

(Figure 11A). Tensile tests were simulated along ND and TD at room temperature, and the resulting stress-strain curves are depicted in Figure 11B. The AB A131 steel exhibited optimal tensile strength and elongation along ND. Assuming the fine-grain regions possess isotropy in mechanical performance with a constant elastic modulus (E_0), the coarse columnar grain was considered anisotropic, with distinct elastic moduli along ND (E_{ND}) and TD (E_{TD}). The relationship of the modulus is:

$$E_{ND} > E_{TD} \approx E_0 \quad \text{(III)}$$

When applying the load on the model along ND, according to the parallel connection principle, the relationship of the stress (σ_{ND}) and strain (ε) could be estimated as:

$$\sigma_{ND} = \frac{2E_0 E_{ND}}{E_0 + E_{ND}}\varepsilon \quad \text{(IV)}$$

When the load was only applied along TD, the σ_{ND}-ε could be assessed as:

$$\sigma_{TD} = \frac{E_0 + E_{TD}}{2}\varepsilon \quad \text{(V)}$$

Uniaxial deformation also induces shear stresses in other directions. To simplify the stress model, the ratio of the stresses along TD and ND can be expressed as:

$$n = \frac{\sigma_{TD}}{\sigma_{ND}} = \frac{(E_0 + E_{ND})(E_0 + E_{TD})}{4E_0 E_{ND}}\varepsilon \quad \text{(VI)}$$

Ideally, since $E_{TD} \approx E_0$, n is generally <1, the tensile stress along ND is expected to be higher than that along TD at the same strain level, suggesting a greater tensile strength in the ND orientation.

After applying the load in ND, the tensile results (Figure 11C) reveal an elliptical deformation profile within the coarse-grain region, attributed to strain-induced boundary migration. The fine-grain region was largely consumed, exhibiting minimal misorientation along TD. Strain mappings indicated a high density of localized shear strain at both ends, suggesting that strain

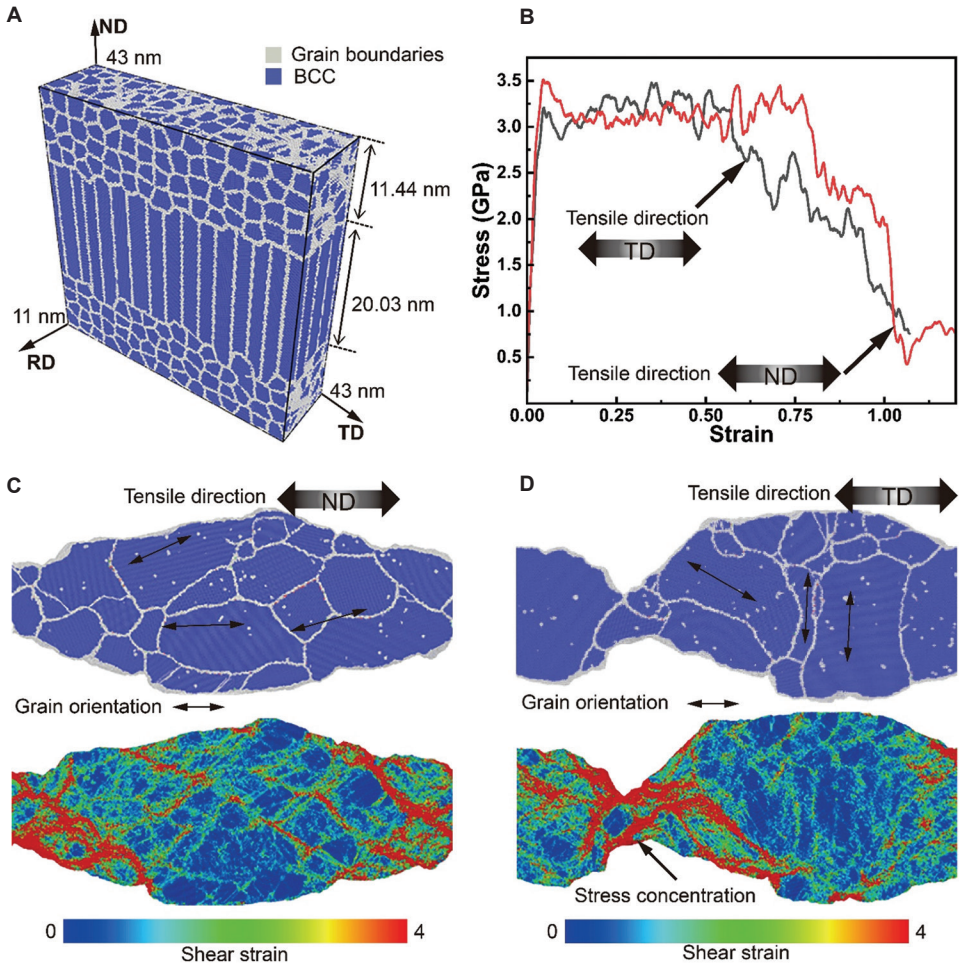

Figure 11. Molecular dynamics (MD) simulation of the heterogeneous structure in AB A131 steel. (A) Model of the heterostructure. (B) Stress-strain curve of the simulation. (C and D) Deformed model and strain mappings along (C) ND and (D) TD
Abbreviations: AB: As-built; ND: Nominal direction; TD: Transverse direction; BCC: Body centered cubic; RD: Roling direction

deformation primarily occurred in the fine-grain region. This behavior contributed to the enhanced tensile strength and high plasticity, consistent with the experiment results of AB-ND.

Under tensile loading in TD, the deformed model (Figure 11D) exhibited an irregular grain profile with notable misorientation along TD. A significant necking phenomenon occurred, characterized by a narrow region where the primary shear strain was concentrated. This suggests uneven deformation and notable stress concentration, which facilitated premature crack initiation and propagation, ultimately reducing tensile strength and elongation. Moreover, the stress concentration also limited the work-hardening capacity under constant loading, consistent with the experimental AB-TD results. Even after HT, HT A131 steel retained the anisotropy performance as tested along different directions, though the heterostructure disappeared. This can be attributed to the optimal crystal orientation along ND (Figures 3B and 7A), which also resulted in significant grain disorientation (Figure S2) and maintained tensile strength differences along different orientations.

5. Conclusion

This study demonstrated the formation of a heterostructure comprising alternative layers of coarse and fine grains in A131 steel fabricated using the DED technique and post-treatment processes. The structure featured notable improvement in strength without the plasticity trade-off. The phase configuration, heterogeneous microstructure, and anisotropy in mechanical performance were thoroughly investigated, with comparisons made to commercial A131 steel. Finally, the formation of the heterostructure and the tensile performance were discussed based on the single-pass deposition and MD simulation, respectively. The main conclusions were summarized as follows:

(i) The AB A131 steel exhibited a high σ_{YS} of 929.5 MPa and σ_{UTS} of 970.4 MPa, approximately 168% and 78% enhancement compared to those of commercial A131 steel (σ_{YS}: 346.5 MPa; σ_{UTS}: 545.0 MPa), with an elongation of 24.5%. After HT, the strength of A131 steel was significantly reduced compared to that before tempering, when retaining 70% enhancement in σ_{YS} compared to commercial A131 steel.

(ii) The A131 steel fabricated by DED methods possesses a significant heterostructure comprising alternating layers of coarse- and fine-grain sections (~300 μm thick), formed due to dendritic growth and thermal cycling. The coarse-grain region mainly consisted of fine columnar grains and acicular martensite, while the fine-grain region featured small equiaxed crystals and fine martensite.

(iii) Tempering treatment of AB A131 steel induced martensite-to-ferrite phase transformation and grain growth into equiaxed structures, reducing crystal misorientation and anisotropy in the microstructure but significantly decreasing mechanical strength.

(iv) The heterostructure induced notable anisotropy in tensile performance, where the tensile properties and hardness of the A131 steel along ND significantly exceeded those in TD. HD had limited impact on reducing anisotropy, even resulting in a 4.6% decrease in σ_{UTS} along TD compared to commercial A131 steel.

(v) MD simulations demonstrated that uniaxial load at ND promoted uniform deformation, enhancing strength and elongation. In contrast, applied load along TD could induce partial stress concentration and necking, reducing both tensile strength and plasticity.

Acknowledgments

None.

Funding

This study was funded by the Guangdong Basic and Applied Basic Research Foundation (2023A1515110594; 2024A1515012049), Shenzhen Science and Technology Program (JCYJ20241202123701003; QTD20210811090146075), and Shenzhen Natural Science Fund (Stable Support Plan Program; GXWD20231129161359002).

Conflict of interest

Yuchao Bai serves as the Guest Editor of the Special Issue, but was not in any way involved in the editorial and peer-review process conducted for this paper, directly or indirectly. Other authors declare they have no competing interests.

Author contributions

Conceptualization: Yuchao Bai
Formal analysis: Jiaming Zhan, Silu Zhang
Investigation: Yuchao Bai, Qi Yan
Methodology: Yuchao Bai, Silu Zhang
Data Curation and Visualization: Qi Yan, Cuiling Zhao
Writing – original draft: Yuchao Bai
Writing – review & editing: Qi Yan, Cuiling Zhao
Funding acquisition: Yuchao Bai

Ethics approval and consent to participate

Not applicable.

Consent for publication

Not applicable.

Availability of data

Data is available from the corresponding author upon reasonable request.

References

1. Kuntanapreeda S, Hess D. Opening access to space by maximizing utilization of 3D printing in launch vehicle design and production. *Appl Sci Eng Prog*. 2021;14(2):143-145.

doi: 10.13316/j.asep/2020/12.002

2. Liu S, Shin YC. Additive manufacturing of Ti6Al4V alloy: A review. *Mater Des*. 2019;164:107552.

doi: 10.1016/j.matdes.2018.107552

3. Liu TS, Chen P, Qiu F, *et al*. Review on laser directed energy deposited aluminum alloys. *Int J Extreme Manuf*. 2024;6(2):022004.

doi: 10.1088/2631-7990/ad16bb

4. Zhang B, Gao Z, Xiao H, Yang X, Li Y, Zhu H. Size effects and optimization during laser directed energy deposition on high thermal conductivity copper alloys. *J Mater Res Technol*. 2024;33:4389-4399.

doi: 10.1016/j.jmrt.2024.10.104

5. Bai Y, Chaudhari A, Wang H. Investigation on the microstructure and machinability of ASTM A131 steel manufactured by directed energy deposition. *J Mater Process Technol*. 2020;276:116410.

doi: 10.1016/j.jmatprotec.2019.116410

6. Gu D, Shi X, Poprawe R, Bourell DL, Setchi R, Zhu J. Material-structure-performance integrated laser-metal additive manufacturing. *Science*. 2021;372(6545):eabg1487.

doi: 10.1126/science.abg1487

7. Seedhouse E, editor. Falcon 9 and falcon heavy. In: *SpaceX: Starship to Mars The First 20 Years*. New York: Springer

International Publishing; 2022. p. 71-93.

8. Materials ASfTa. *ASTM A131/A 131M-04. Standard Specification for Structural Steel for Ships*. Commonwealth of Pennsylvania: ASTM International; 2004.

9. Sirisatien T, Mahabunphachai S, Sojiphan K. Effect of submerged arc welding process with one-side one-pass welding technique on distortion behavior of shipbuilding steel plate ASTM A131 grade A. *Mater Today Proc*. 2018;5(3, Part 2):9543-9551.

   doi: 10.1016/j.matpr.2017.10.136

10. Yan Q, Chen B, Kang N, *et al*. Comparison study on microstructure and mechanical properties of Ti-6Al-4V alloys fabricated by powder-based selective-laser-melting and sintering methods. *Mater Charact*. 2020;164:110358.

    doi: 10.1016/j.matchar.2020.110358

11. Yan Q, Chen B, Jia Z, *et al*. Formation of dual quasi-continuous networked structure and its strengthening effect in Ti-6Al-4V alloy reinforced with graphene via powder bed fusion. *Add Manuf*. 2024;92:104364.

    doi: 10.1016/j.addma.2024.104364

12. Bai Y, Yan Y, Chen J, Liang C, Bi G, Zhao C. Microstructure and mechanical property evolution of 316L/18Ni300 bimetallic structure manufactured by laser powder bed fusion. *Mater Sci Eng A*. 2025;929:148141.

    doi: 10.1016/j.msea.2025.148141

13. Ang LJJ, Huang J, Nai MLS, Wang P. Additive manufacturing techniques for EH36 steels: Challenges and future directions. *ESAM*. 2025;1(1):025060005.

    doi: 10.36922/esam025060005

14. Wenjin W, Beng TS, Kai CC, *et al*. Preliminary investigation on SLM of ASTM A131 EH36 high tensile strength steel for shipbuilding applications. *Proceedings of the 2nd International Conference on Progress in Additive Manufacturing*; 2014.

    doi: 10.3850/978-981-09-0446-3_083

15. Wu W, Tor SB, Merchant AA. Tensile properties of ASTM A131 EH36 shipbuilding steel processed by selective laser melting. *Proceedings of the 3rd International Conference on Progress in Additive Manufacturing*; 2018.

16. Wang J, Wu WJ, Jing W, *et al*. Improvement of densification and microstructure of ASTM A131 EH36 steel samples additively manufactured via selective laser melting with varying laser scanning speed and hatch spacing. *Mater Sci Eng A*. 2019;746:300-313.

    doi: 10.1016/j.msea.2019.01.019

17. Wang J, Chew YX, Wu WJ, *et al*. Microstructure and mechanical properties of ASTM A131 EH36 steel fabricated by laser aided additive manufacturing. *Mater Charact*. 2021;174:110949.

    doi: 10.1016/j.matchar.2021.110949

18. Wang J, Zhang M, Wang B, *et al*. Influence of surface porosity on fatigue life of additively manufactured ASTM A131 EH36 steel. *Int J Fatigue*. 2021;142:105894.

    doi: 10.1016/j.ijfatigue.2020.105894

19. Liu L, Li S, Pan D, *et al*. Loss-free tensile ductility of dual-structure titanium composites via an interdiffusion and self-organization strategy. *Proc Natl Acad Sci U S A*. 2023;120(28):e2302234120.

    doi: 10.1073/pnas.2302234120

20. Gao S, Li Z, Van Petegem S, *et al*. Additive manufacturing of alloys with programmable microstructure and properties. *Nat Commun*. 2023;14(1):6752.

    doi: 10.1038/s41467-023-42326-y

21. Tan C, Li R, Su J, *et al*. Review on field assisted metal additive manufacturing. *Int J Mach Tools Manuf*. 2023;189:104032.

    doi: 10.1016/j.ijmachtools.2023.104032

22. Svetlizky D, Das M, Zheng B, *et al*. Directed energy deposition (DED) additive manufacturing: Physical characteristics, defects, challenges and applications. *Mater Today*. 2021;49:271-295.

    doi: 10.1016/j.mattod.2021.03.020

23. Kong H, Yibo L, Fuxiang L, *et al*. *In situ* fabrication of martensitic stainless steel via heterogeneous double-wire arc-directed energy deposition. *Virt Phys Prototyp*. 2024;19(1):e2350610.

    doi: 10.1080/17452759.2024.2350610

24. Myers MB, Bandyopadhyay A. Understanding the antibacterial efficacy of additively manufactured copper-added 316L stainless steel. *MSAM*. 2025;4(1):7357.

    doi: 10.36922/msam.7357

25. Zuckschwerdt NW, Bandyopadhyay A. Multi-material structures of Ti6Al4V and Ti6Al4V-B4C through directed energy deposition-based additive manufacturing. *MSAM*. 2024;3(3):3571.

    doi: 10.36922/msam.3571

26. Su J, Li Q, Teng J, *et al*. Programmable mechanical properties of additively manufactured novel steel. *Int J Extreme Manuf*. 2025;7(1):015001.

    doi: 10.1088/2631-7990/ad88bc

27. Dan X, Ren C, Song Z, *et al*. Exceptional strength and ductility in heterogeneous multi-gradient TiAl alloys through additive manufacturing. *Acta Mater*. 2024;281:120395.

    doi: 10.1016/j.actamat.2024.120395

28. Wu X, Yang M, Yuan F, *et al*. Heterogeneous lamella structure unites ultrafine-grain strength with coarse-grain ductility. *Proc Natl Acad Sci U S A*. 2015;112(47):14501-14505.

    doi: 10.1073/pnas.1517193112

29. Li D, Fan G, Huang X, *et al*. Enhanced strength in pure Ti via design of alternating coarse- and fine-grain layers. *Acta Mater*. 2021;206:116627.

    doi: 10.1016/j.actamat.2021.116627

30. Tan C, Li Q, Yao X, *et al*. Machine learning customized novel material for energy-efficient 4D printing. *Adv Sci*. 2023;10(10):2206607.

    doi: 10.1002/advs.202206607

31. National Standardization Administration of the People's Republic of China. *GB/T 36165-2018. Determination of Average Grain Size of Metal -- Electron Backscatter Dirffraction (EBSD) Method*. Beijing: National Standardization Administration of the People's Republic of China; 2018.

32. Plimpton S. Fast parallel algorithms for short-range molecular dynamics. *J Comput Phys*. 1995;117(1):1-19.

    doi: 10.1006/jcph.1995.1039

33. Zhan JM, Yao XH, Han F. An approach of peridynamic modeling associated with molecular dynamics for fracture simulation of particle reinforced metal matrix composites. *Compos Struct*. 2020;250:112613.

    doi: 10.1016/j.compstruct.2020.112613

34. Proville L, Choudhury A. Unravelling the jerky glide of dislocations in body-centred cubic crystals. *Nat Mater*. 2024;23(1):47-51.

    doi: 10.1038/s41563-023-01728-5

35. Etesami SA, Asadi E. Molecular dynamics for near melting temperatures simulations of metals using modified embedded-atom method. *J Phys Chem Solids*. 2018;112:61-72.

    doi: 10.1016/j.jpcs.2017.09.001

36. Lim H, Hale LM, Zimmerman JA, Battaile CC, Weinberger CR. A multi-scale model of dislocation plasticity in α-Fe: Incorporating temperature, strain rate and non-schmid effects. *Int J Plastic*. 2015;73:100-118.

    doi: 10.1016/j.ijplas.2014.12.005

37. Vasques CMA, Cavadas AMS, Abrantes JCC. Technology overview and investigation of the quality of a 3D-printed maraging steel demonstration part. *MSAM*. 2025;4(2):025040002.

    doi: 10.36922/msam025040002

38. Li W, Yan L, Chen X, Zhang J, Zhang X, Liou F. Directed energy depositing a new Fe-Cr-Ni alloy with gradually changing composition with elemental powder mixes and particle size' effect in fabrication process. *J Mater Proc Technol*. 2018;255:96-104.

    doi: 10.1016/j.jmatprotec.2017.12.010

39. Donizete Borba TM, Wagner DF, Leonardo DOT, Cardoso R Jr. Assessment of the weldability of EH36 TMCP shipbuilding steel welded by high heat input submerged arc welding. *Weld Int*. 2017;31(3):184-195.

    doi: 10.1080/09507116.2016.1218619

40. Potez L, Lapasset G, Kubin L. Jerky flow (the PLC effect) in Ll2 Al3Ti-based alloys. *Scr Metallurgica Mater*. 1992; 26(5):841-846.

    doi: 10.1016/0956-716X(92)90449-O

41. Hsu WC, Shen TE, Liang YC, Yeh JW, Tsai CW. *In situ* analysis of the portevin-le chatelier effect from low to high-entropy alloy in equal HfNbTaTiZr system. *Acta Mater*. 2023;253:118981.

    doi: 10.1016/j.actamat.2023.118981

42. Ananthakrishna G. Current theoretical approaches to collective behavior of dislocations. *Phys Rep*. 2007; 440(4-6):113-259.

    doi: 10.1016/j.physrep.2006.10.003

43. Sarkar A, Maloy SA, Murty KL. Investigation of portevin-le chatelier effect in HT-9 steel. *Mater Sci Eng A*. 2015;631:120-125.

    doi: 10.1016/j.msea.2015.02.022

44. Vahedi Nemani A, Ghaffari M, Nasiri A. Comparison of microstructural characteristics and mechanical properties of shipbuilding steel plates fabricated by conventional rolling versus wire arc additive manufacturing. *Add Manuf*. 2020;32:101086.

    doi: 10.1016/j.addma.2020.101086

45. Chen ZW, Phan MAL, Darvish K. Grain growth during selective laser melting of a co-cr-mo alloy. *J Mater Sci*. 2017;52(12):7415-7427.

    doi: 10.1007/s10853-017-0975-z

46. Kok Y, Tan XP, Wang P, *et al*. Anisotropy and heterogeneity of microstructure and mechanical properties in metal additive manufacturing: A critical review. *Mater Des*. 2018;139:565-586.

    doi: 10.1016/j.matdes.2017.11.021